

Spray formation: a numerical closeupYue Ling,¹ Daniel Fuster,¹ Gretar Tryggvason,² and Stéphane Zaleski¹¹*Institut Jean le Rond d'Alembert, Sorbonne Univ, UPMC Univ Paris 06, CNRS, UMR 7190, F-75005, Paris, France*²*Department of Aerospace & Mechanical Engineering, University of Notre Dame, Notre Dame, IN 46556, United States*

Spray formation and atomization in a gas-liquid mixing layer is an important fundamental problem of multiphase flows. It is highly desirable to visualize the detailed atomization process and to analyze the instabilities and mechanisms involved, and massive numerical simulations are required, in addition to experiment. Rapid development of numerical methods and computer technology in the past decades now allows large-scale three-dimensional direct numerical simulations of atomization to be performed. Nevertheless, the fundamental question, whether all the physical scales involved in the primary breakup process are faithfully resolved, remains unclear. In the present study, we conduct direct numerical simulations of spray formation in a gas-liquid mixing layer with state-of-the-art computational resources (using up to 4 billion cells and 16384 cores), in order to obtain a high-fidelity numerical closeup of the detailed mechanisms of spray formation. We also aim to examine whether present computational resources are sufficient for a fully resolved direct numerical simulation of atomization.

I. INTRODUCTION

The breakup of fluid masses is a phenomenon of enormous complexity, with diverse physical setups and mechanisms. When the fluid masses break rapidly into large numbers of small droplets one speaks of atomization^{1,2}. Such atomization in a gas-liquid mixing layer, where a high-speed gas stream emerges from an orifice parallel to a lower-speed liquid stream, has been studied in great detail^{3,4}. The resulting Kelvin-Helmholtz instability generates large coherent structures that grow in size as they propagate downstream, together with equally growing wave-like structures⁵ on the liquid-gas interface. The standard picture of atomization¹ is that two-dimensional wave structures form near the orifice, develop into sheets, which in turn develop Taylor-Culick end rims. The flow then becomes more markedly three dimensional: finger branching from the end rim, and then various thread, fibers or ligament-like structures parallel to the flow appear, which eventually break into droplets. This sequence and its variants are called *primary* atomization, which is supposed to be followed by *secondary* atomization, the breakup of large drops further downstream whenever they interact with sufficiently high-velocity gas flow. Several types of probability distributions of droplet sizes have been proposed and compared to experiments^{3,6}. Another mechanism for primary atomization is the formation of holes in the thin-sheet-like structures that appear in the waves prior to the formation of ligaments and fingers. These holes-in-thin-sheets structures are quite similar, but not identical, to the holes that form in bag-breakup secondary atomization⁷ and droplet impact⁸. The hole formation has not been visualized as frequently in primary atomization and is thus less firmly documented.

In order to better understand the mechanisms underlying atomization, experimentalists have switched from the coaxial round jets typical of industrial applications to a quasi-planar setup that is more favorable for detailed analysis⁹⁻¹¹. This setup has allowed precise measurements and detailed visualizations of the droplet-forming process. In the quasi-planar configuration it is possible to compare the growth and frequency of the Kelvin-Helmholtz instability in the linear regime as predicted by numerical simulation, linear stability theory and experiments¹². Three-dimensional analysis is, for obvious reasons¹³⁻¹⁵, less advanced, despite a large number of results in the references already cited. In this work we simulate a model of the quasi-planar experiment of Matas *et al.*⁹ in order to better understand the mechanisms of droplet formation.

II. NUMERICAL METHOD AND SIMULATION SETUP

The computational setup is shown in Figure 1. The domain is a box of dimensions $L_x \times L_y \times L_z$, where we inject two streams, liquid and gas, separated by a solid separator plate of size $\ell_x \times \ell_y \times L_z$. The streams enter through the boundary at $x = 0$ with velocities U_l and U_g , respectively. The thickness of the liquid stream is H while that for the gas stream is $H - \ell_y$. The thickness of the boundary layers on the liquid and gas sides of the separator plate are taken to be identical and denoted by δ , and we take $\delta = H/4$. The length ℓ_x and the thickness ℓ_y of the separator plate are $H/2$ and $H/32$, respectively and it has been shown that the details of the separator plate is immaterial to the atomization process as long as $\ell_y \ll \delta$.¹² The domain is initially filled with gas and then liquid progressively enters it. In order to minimize the effect of the finite size of the domain, the dimensions of the box are large in the x and y dimensions $L_x = 16H$ and $L_y = 8H$ (while L_z is set to $2H$). Special care is taken to specify exit conditions to minimize the recirculating flow and avoid excessive reinjection of coherent structures near the inlet.

It is not possible with the present computational capability and numerical methodology to perform direct numerical simulations (DNS) in this setup using the physical parameters (such as the large liquid-to-gas density ratio) exactly as in the experiments⁹. This is due to the very wide range of relevant physical scales. Indeed the tiny submicron droplets generated are three orders of magnitudes smaller than H . To alleviate these problems we reduce the physical scale ($H = 0.8$ mm is used here compared to $H = 5$ to 20 mm in experiments⁹) and choose a set of parameters that allows faster and easier simulations while still placing the flow in the high-speed atomization regime. The physical parameters and the corresponding dimensionless parameters are given in Tables I and II, using standard notations and international units.

ρ_l	ρ_g	μ_l	μ_g	σ	$U_{0,l}$	$U_{0,g}$	H	δ_g	ℓ_x
(kg/m^3)	(kg/m^3)	($Pa\ s$)	($Pa\ s$)	(N/m)	(m/s)	(m/s)	(m)	(m)	(m)
1000	50	10^{-3}	5×10^{-5}	0.05	10	0.5	8×10^{-4}	2×10^{-4}	2.5×10^{-5}

TABLE I. Physical parameters.

We solve the Navier-Stokes equations for incompressible flow with sharp interfaces and constant surface tension. The fields are discretized using a fixed regular cubic grid (with cell

M	r	m	$\text{Re}_{g,\delta}$	$\text{We}_{g,\delta}$	Re_g
$\rho_g U_g^2 / (\rho_l U_l^2)$	ρ_l / ρ_g	μ_l / μ_g	$\rho_g U_g \delta / \mu_g$	$\rho_g U_g^2 \delta / \sigma$	$\rho_g U_g H / \mu_g$
20	20	20	2000	20	8000

TABLE II. Key dimensionless parameters.

size denoted by Δ), and we use a projection method for the time stepping to incorporate the incompressibility condition. The interface is tracked using a Volume-of-Fluid (VOF) method with a Mixed Youngs-Centered Scheme to determine the normal vector and a Lagrangian-Explicit scheme for the VOF advection¹⁶. The advection of momentum near the interface is conducted in a manner consistent with the VOF advection¹⁷ with the superbee limiter applied in flux calculation. The viscous term is treated explicitly. Curvature is computed using the height-function method¹⁸. Surface tension is computed from curvature by a well-balanced Continuous-Surface-Force method^{18,19}. Density and viscosity are computed from the VOF fraction by an arithmetic mean. To capture the dynamics of poorly resolved droplets accurately, droplets of size smaller than 4 cells are converted to Lagrangian point-particles²⁰. The overall method is implemented in the free code *PARIS*²¹ and validation studies can be found in Ling *et al.*²⁰.

To assess whether the present simulation is a full DNS of atomization, simulations are performed on four grids called M0, M1, M2, and M3 so that Mn has $H/\Delta = 32 \times 2^n$ points in the liquid layer H . For the M3 mesh, the simulation was performed on about 4 billion cells using 16,384 processors. The total simulation time for all four meshes took over 10 million CPU hours. The results presented correspond to the M3 mesh, unless stated otherwise.

Run	$\Delta(\mu\text{m})$	H/Δ	Cells #	Cores #	Total core-hrs
M0	25	32	8.39×10^6	32	$\sim 3 \times 10^3$
M1	12.5	64	6.71×10^7	256	$\sim 5 \times 10^4$
M2	6.25	128	5.37×10^8	2048	$\sim 1 \times 10^6$
M4	3.125	256	4.29×10^9	16384	$\sim 10 \times 10^6$

TABLE III. Summary of simulation runs.

III. RESULTS

A. Overall atomization process

A global view of the atomization in a gas-liquid mixing layer is shown in Fig. 1. The single-phase (gas-gas) and the two-phase (gas-liquid) mixing layers can be identified from the z -vorticity plotted on the backplane. Both of the mixing layers are unstable due to the velocity difference across the layers. The gas-liquid mixing layer develops faster and evolves a Kelvin-Helmholtz-like wave on the interface. The interfacial wave grows and a thin liquid sheet forms at the wave crest. A Taylor-Culick rim appears at the edge of the liquid sheet. The sheet folds and creases under the action of the gas turbulence, and this leads to perturbations of the rim. These perturbations produce small fingers which later develop into long ligaments. There is an important difference between the rim instabilities observed here and those seen for example in droplet splashes where interaction with energetic air motion is absent. The ligaments eventually break into small droplets due to Rayleigh-Plateau instability. The unbroken part of the liquid sheet reattaches to the domain bottom. Compared to the gas-liquid mixing layer, the gas-gas mixing layer evolves more slowly. The invasion of the turbulent vortices from the gas-liquid mixing layer accelerates the development the gas-gas mixing layer. Eventually, the two mixing layers merge and the downstream flows become fairly violent and chaotic.

B. Formation of sheets

Due to the velocity difference between the gas and liquid across the interface, a Kelvin-Helmholtz-like wave develops on the interface and propagates downstream. As the interfacial wave grows the radius of curvature at the wave crest continues to decrease and eventually liquid sheets form.

It is generally believed that the wave that appears first is a two-dimensional one and then transverse instabilities (such as Rayleigh-Taylor (RT) and Rayleigh-Plateau (RP) instabilities) develop at the rim of the liquid sheet. This quasi-2D wave and its development are shown in Figs. 2 (a)-(d). The temporal evolution of the wave can be seen more clearly by a sequence of snapshots of the interface at the plane $z = H$ (see Fig. 2 (e)). The wave initially takes an Gaussian-like shape. The minimum radius of curvature is located near the

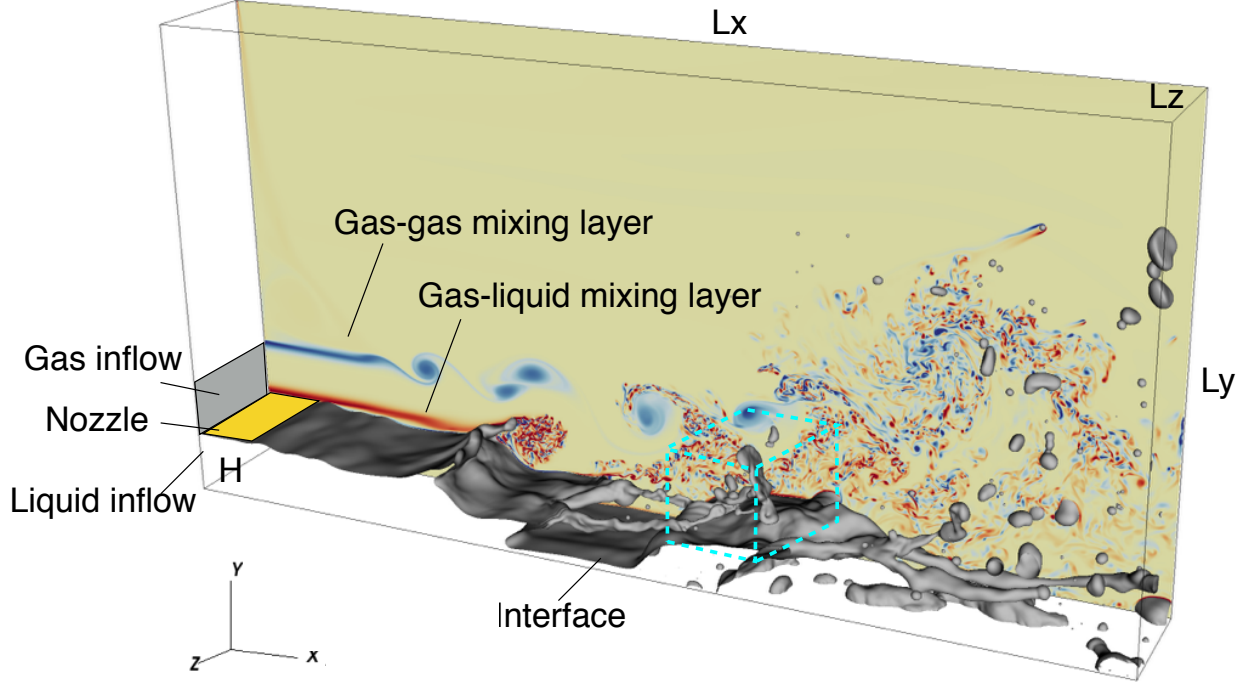


FIG. 1. Spray formation and atomization in a gas-liquid mixing layer. The z -vorticity is shown on the backplane. The sampling region for droplets statistics is indicated by cyan lines.

wave crest, and decreases from $189.7 \mu\text{m}$ at 17.3 ms to $43.1 \mu\text{m}$ at 17.6 ms . Then the wave tends to fold forward. At a time between 17.7 and 17.9 ms , the two interfaces on both sides of the wave crest become parallel and form a liquid sheet. At this point, the thickness of the liquid sheet, denoted by e , is $174 \mu\text{m}$. As the sheet is pulled and stretched by the fast gas stream, its thickness decreases in time. At $t = 18.2 \text{ ms}$ (the last profile in Fig. 2(e)) the minimum sheet thickness decreases to $e_{\min} = 49.2 \mu\text{m}$. At this scale the capillary time is $\tau_{ca} = (\rho_l e^3 / \sigma)^{1/2} \approx 0.05 \text{ ms}$ and the Ohnesorge number is $\text{Oh} = \mu_l (\sigma \rho_l e)^{-1/2} \approx 0.02$. There are still $e/\Delta = 16$ grid points for the sheet thickness. It is seen that at this time of $t = 18.2 \text{ ms}$ the tip of the liquid sheet starts to fold. The radius of curvature at the hinge point is about $22 \mu\text{m}$. The fact that the tip of the sheet folds, instead of forming a Taylor-Culick end rim as expected for this time scale and Oh number, is a testimony of the strong interaction of the liquid sheet with the gas stream. The wave amplitude at $t = 18.2 \text{ ms}$ is comparable to H bringing the interaction to a maximum.

The celerity of the interfacial wave is approximately a constant, which agrees well with

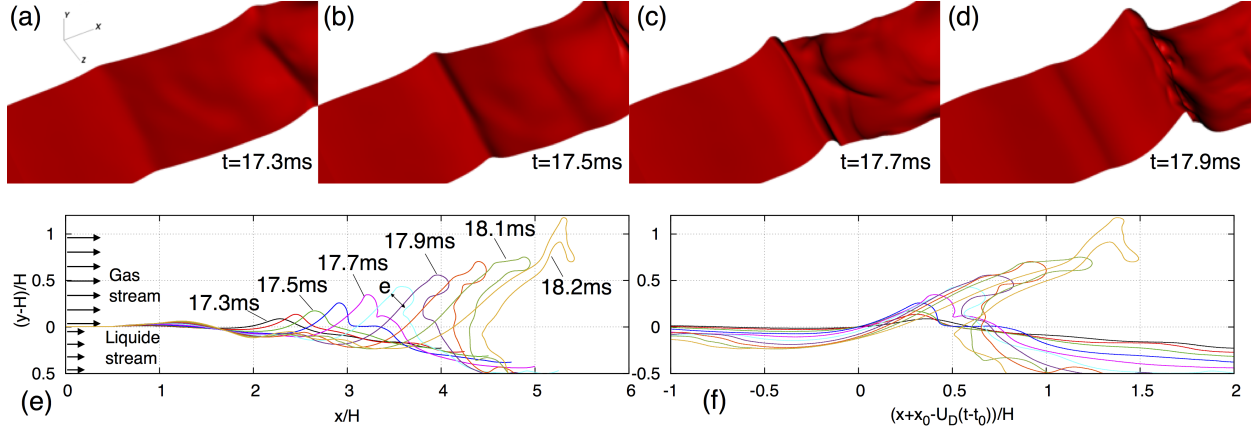


FIG. 2. Development of a quasi-2D interfacial wave, forming a liquid sheet: (a)-(d) time snapshots of the interface; interface profiles at plane $z = H$ with (e) original scale and (f) x -axis scaled by the Dimotakis speed U_D .

the Dimotakis speed,

$$U_D = \frac{U_l + \sqrt{r}U_g}{1 + \sqrt{r}}, \quad (1)$$

which is about 2.23 m/s for the present case. If the x -axis is shifted by U_D with respect to the origin of wave formation x_0 and t_0 , the waves at different times collapse, except the amplitude, as shown in Fig. 2(f). This is similar to the well documented 2D case¹⁰.

Beyond the conventionally known quasi-2D waves, it is observed from the simulation results that the liquid sheet also forms in a fully three-dimensional manner (see Figs. 3 (a)-(d)), resulting in a significant transversely deforming rim at the sheet edge. This transverse wavelength is of the order of the width of the domain. (This may indicate that the domain width is too small for the long wavelength modes in transverse instability.) It has been shown before that the Rayleigh-Plateau instability can induce transverse deformation of the rim, which later develops into fingers^{22,23}. However, here the formation of 3D structures is clearly much faster than the Rayleigh-Plateau rim instability would be, and even occurs before the rim is formed at about $t = 19.6$ ms in Fig. 3 (c).

Other different mechanisms can contribute to the formation of the 3D wave. In particular, it has been shown by the transient growth theory that the 3D perturbations of a two-phase mixing layer can be more unstable than the 2D ones²⁴. Furthermore, the turbulent gas flow on top of the interface impose significant 3D forcing on the interfacial wave. See the turbulent vortical structures and their “foot prints” on the interface in Figs. 3(e) and (f).

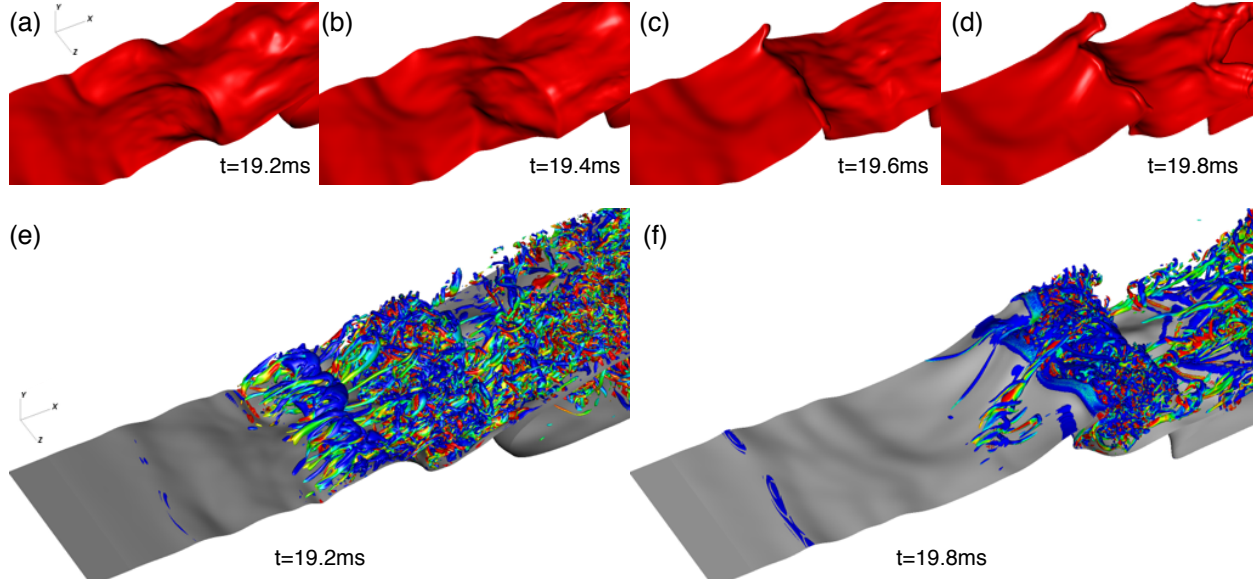


FIG. 3. Development of a fully 3D interfacial wave: (a)-(d) time snapshots of the interface and (e)-(f) turbulent vortical structures in the gas-liquid mixing layer (visualized by the λ_2 criterion).

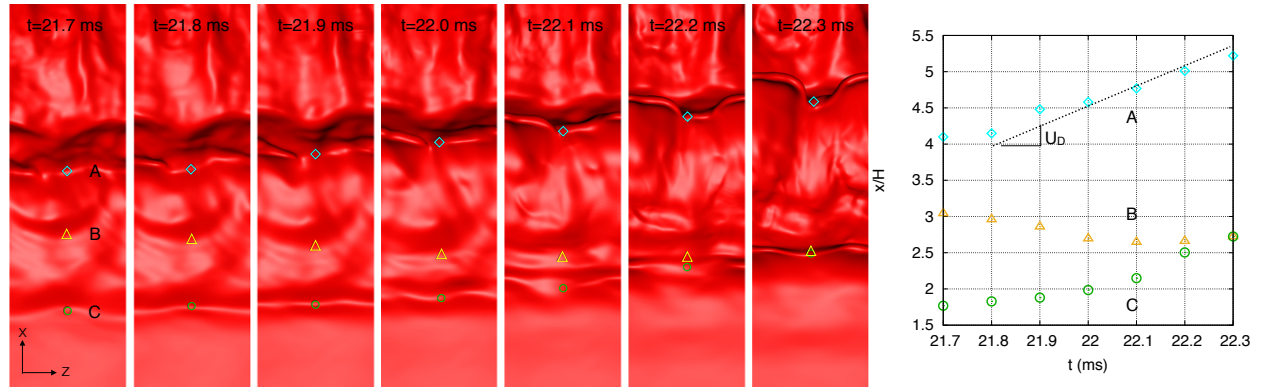


FIG. 4. Interfacial waves interaction (results by M2 mesh). Symbols indicate locations of the wave crests at plan $z = H$. The Dimotakis speed (black dashed line) is plotted for comparison.

Finally, complex capillary wave interactions on the interface also contribute to triggering irregular 3D waves. As shown in Fig. 4, the capillary waves propagate both upstream (waves A and C) and downstream (wave B). The upstream and downstream propagating waves B and C meet and accelerate the development of the C wave.

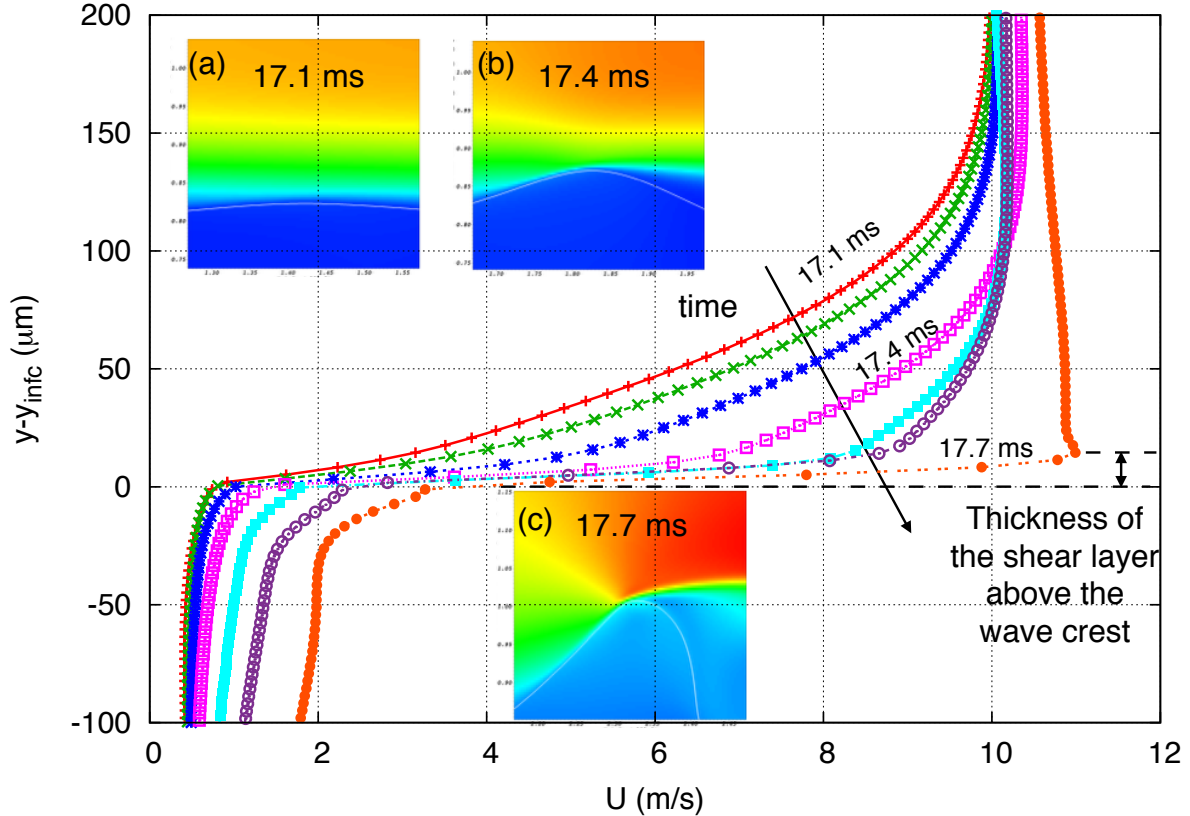


FIG. 5. Temporal evolution of the shear layer near the wave crest. (a)-(c) Streamwise velocity contours near the wave crest (gas-liquid interfaces are indicated by white lines). The line plots are the streamwise velocity profiles in y direction at the wave crest. The y location of the interface is denoted by y_{inf} .

C. Effect of mesh resolution

It has been shown previously that the boundary layer of the injected gas stream must be well resolved, since otherwise the gas-assisted atomization and the frequency of the interfacial instability will not be accurately captured¹². In the present study, we found that requiring sufficient numerical resolution to compute the formation of the sheet and the rim indeed introduce a stricter requirement on mesh size. As shown in Fig. 2(b), the radii of the wave crest can go down to about $43.1 \mu\text{m}$ ($t = 17.6 \text{ ms}$) or even lower to $22 \mu\text{m}$ when the sheet folds, which is much smaller than the injected gas boundary layer thickness δ ($\approx 200 \mu\text{m}$). Furthermore, the thickness of the shear layer above the wave crest significantly decreases as the wave develops, see Fig. 5. The shear layer thickness is initially similar to the boundary

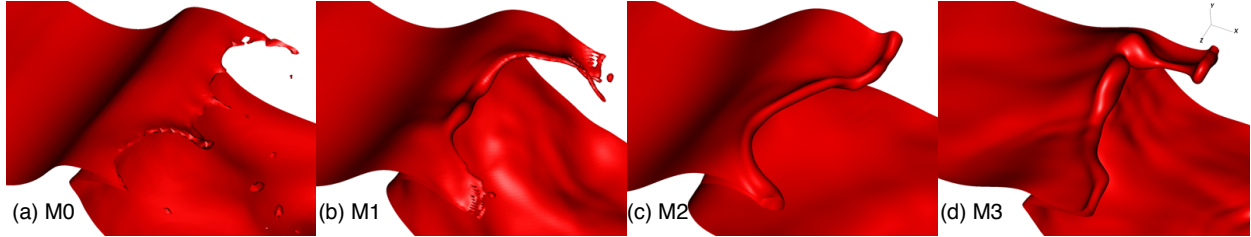


FIG. 6. A closeup at sheet formed at the wave crest for different mesh resolution.

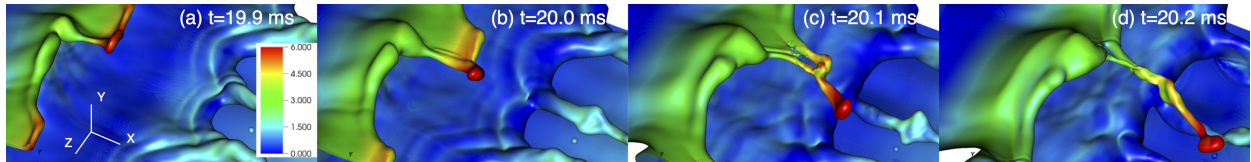


FIG. 7. Ligaments formation due to fingering at the tip of a liquid sheet. The color on the interface indicates the streamwise velocity.

layer thickness of the injected gas stream δ (see $t = 17.1$ ms), then it drops rapidly as the wave grows to about $15 \mu\text{m}$ at $t = 17.7$ ms. The M0 mesh ($\Delta = 25 \mu\text{m}$) is clearly insufficient to resolve the wave crest curvature and the shear layer, as a result, the formation of the sheet is not properly captured. As shown in Fig. 6(a), the rim is completely missed and the tip of liquid sheet breaks erroneously, forming numerous tiny ligaments and droplets. The result for M1 ($\Delta = 12.5 \mu\text{m}$) is better but two sides of the rim are still poorly resolved. For M2 and M3 meshes ($\Delta = 6.25$ and $3.125 \mu\text{m}$), about 4 and 7 cells are used to resolve the minimum radius of the wave and about 3 and 6 cells for the shear layer above the wave crest. As a result, the sheet formation and the rim dynamics are well captured, see Figs. 6(c)-(d). In such cases, no fingers or droplets are formed at this early stage.

D. Formation of ligaments

The transverse instability of the rim is known to generate fingers at the tip of a liquid sheet²³. The formation of a finger at the rim is well captured by the present simulation as shown in Fig. 7. The streamwise fluid velocity is also plotted on the interface and it is seen that the velocity increases gradually from the base to the round tip of the finger, indicating that the finger is stretched by the surrounding fast gas stream. Eventually the short finger develops into a long ligament, which breaks later to form droplets.

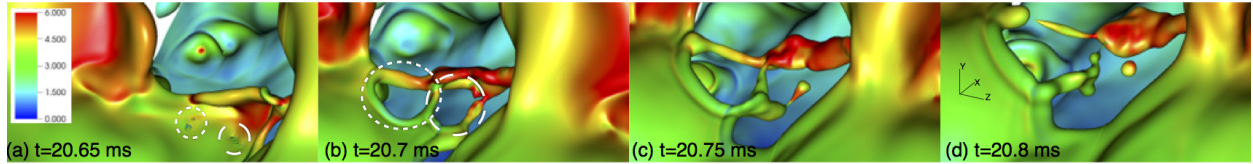


FIG. 8. Ligaments formation due to holes in a liquid sheet. The color on the interface indicates the streamwise velocity.

Beyond fingering at the rim of the liquid sheet, holes appearing in the liquid sheet are observed to be another way to break the liquid sheet and to produce ligaments. Similar to the fingers, the liquid sheet is also stretched by the gas stream and becomes thinner and thinner. At a certain stage, holes are formed in the liquid sheet, see Fig. 8. The two holes are initially very small (highlighted by different dashed lines) but later they expand rapidly, causing the liquid sheet to rupture. Several small ligaments are generated and the orientations of these ligaments are more diverse, different from the ligaments formed by fingering which tend to align with the streamwise direction.

For a stationary liquid sheet, holes are formed only when the sheet thickness is very small ($e \sim O(10)\text{nm}$) and the disjoining pressure becomes active. For a dynamic liquid sheet it has been shown in recent experiments that holes can form at a much larger thickness ($e \sim O(10)\mu\text{m}$)^{7,8}. For example, in the experiment of Marston *et al.*⁸, the sheet thickness estimated by the hole expansion velocity and the Taylor-Culick theory is about 9 to 16 μm . Several effects may explain the piercing of a liquid sheet at such large thicknesses, and among them are Marangoni effects and perturbations from bubbles or droplets too small to be visible. Random perturbations from unseen objects are difficult to model, and Marangoni forces are not included in the present simulation. Here holes appear when the thickness of the liquid sheet decreases to about the cell size Δ . This numerical cut-off length scale (the smallest Δ used is about 3.1 μm) is much larger than breakup thickness of a stationary sheet but is comparable or even smaller than the length at which dynamic liquid sheets are seen to break in experiments.

The evolution of a hole formed in a liquid sheet is shown in Fig. 9. The measured hole expansion velocities in the streamwise and transverse directions are $U_{h,x} \approx 2.70$ m/s and $U_{h,z} \approx 0.978$ m/s, respectively. As can be seen from the cross sections of the hole in the $y-z$ and $x-y$ planes, the sheet thickness near the hole is very uneven. The minimum

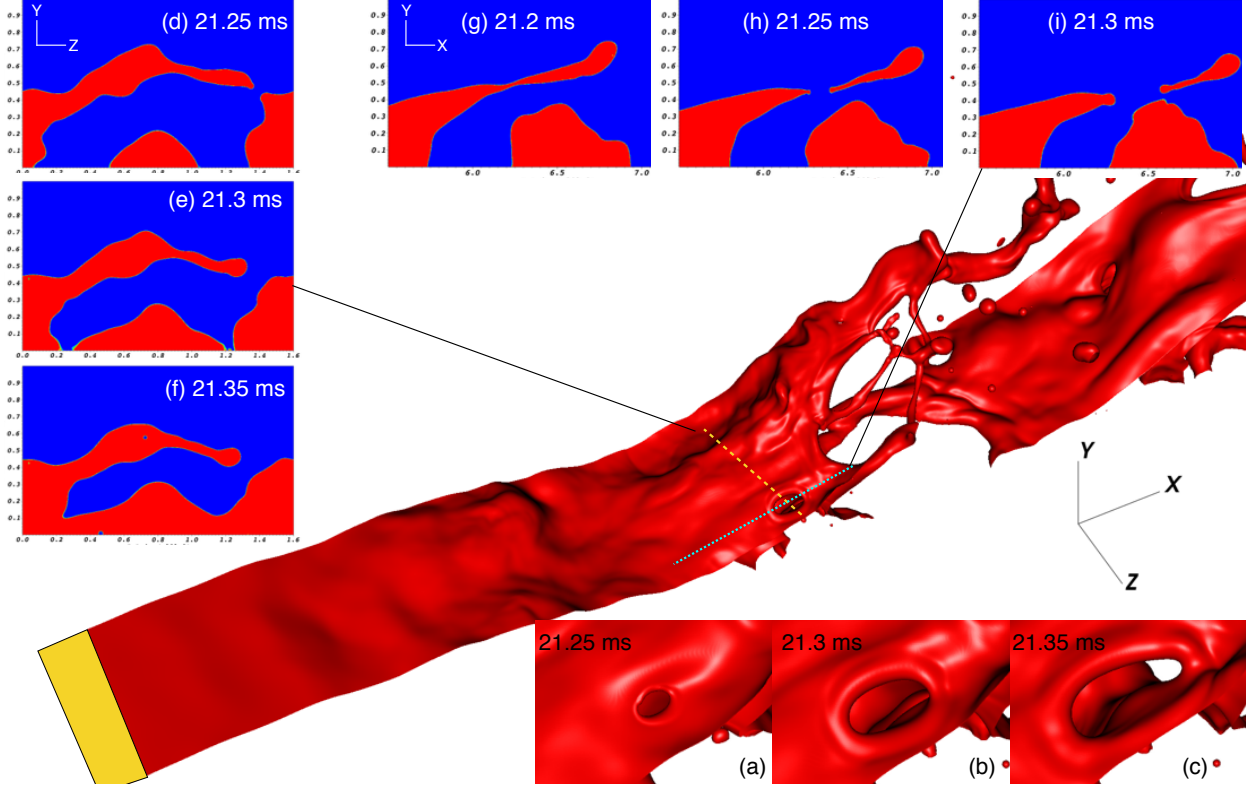


FIG. 9. Evolution of a hole formed in a liquid sheet. (a)-(c) A closeup a the hole expansion. Liquid volume fraction (red) at $y - z$ and $y - x$ planes cutting through the holes are also shown in (d)-(f) and (g)-(i), respectively.

sheet thickness just before the hole appears is about $22 \mu\text{m}$, and after the sheet rupture the thickness in the vicinity of the hole varies from 27 to $85 \mu\text{m}$. The Taylor-Culick velocity,

$$U_{h,TC} = \sqrt{\frac{2\sigma}{\rho l e}} \quad (2)$$

can be calculated based on the sheet thickness, yielding $U_{h,TC} = 0.95 \sim 1.68 \text{ m/s}$. It is seen that $U_{h,z}$ agrees well with $U_{h,TC}$. The excess of $U_{h,x}$ over the Taylor-Culick prediction is due to the streamwise stretching the liquid sheet, which causes the hole to expand faster in the x than in the z direction.

Since mechanisms of sheet rupture, such as disjoining pressure, are absent in the present study, the initial formation of the holes is mesh dependent. However, it is quite clear that the subsequent hole development and the rim around the hole are well resolved with the M3 mesh. As a consequence, further increase of mesh resolution will only delay the pinch-off point but will not affect the ligaments formed from the expansion of the holes.

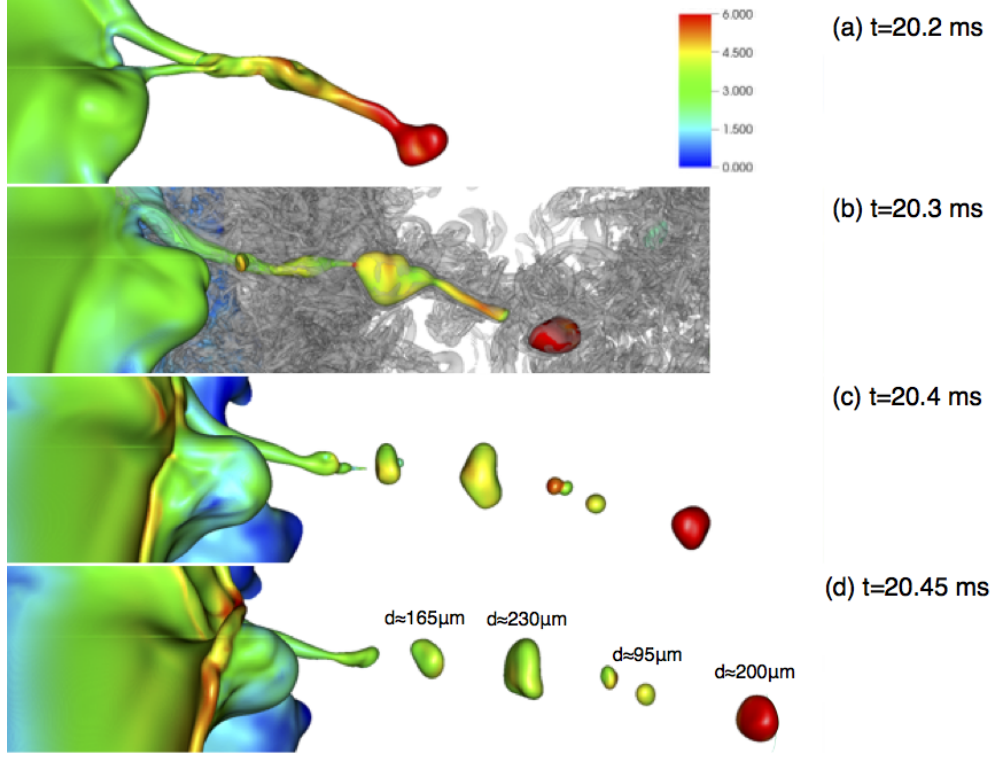


FIG. 10. Droplets generation due to ligament breakup. The turbulent vortices surrounding the ligament is plotted in (b) by the λ_2 criterion.

E. Formation of droplets

Eventually the ligaments break into small droplets and one realization of the breakup process is shown in Fig. 10. The ligament here is the same one as shown in Fig. 7. The ligament exhibits a very irregular shape compared to typical Rayleigh-Plateau breakup of a stationary ligament. The ligament diameter varies from 72 to 244 μm along its axis. The stretching by the surrounding turbulent gas stream (see Fig. 10(b)) clearly contributes to the irregular breakup. The neck behind the tail of the ligament pinches off, forming a big droplet of $d \approx 200\mu\text{m}$. The retraction of the ligament tail from the pinch-off point forms a big liquid blob in the middle of the ligament. Similar behavior is also observed in experiments³. Coalescence of small droplets are also seen in Fig. 10(c). At the end, a series of droplets varying from 95 to 230 μm are produced.

To have a more general analysis of the droplets formed in atomization, we investigate the size distribution of droplets in a cubic box located downstream of the breaking wave. The sampling region is indicated in Fig. 1. The edge length of the cubic box is $2H$ ($8 \leq x/H \leq 10$,

$0.5 \leq y/H \leq 2.5$, and spanning the whole width of the domain). The sampling is conducted after the atomization has reached a statistically steady state and over time intervals of 48, 21, 27, and 4.6 ms for the M0, M1, M2, and M3 meshes, respectively. (The sampling time for M3 mesh is significant shorter due to the extremely high computational cost.) The average number of droplets $n_d(d)$ as a function of droplet volume-based diameter is plotted in Fig. 11(a), where $n_d(d)$ is defined as

$$n_d(d) = \frac{N(d)}{N_s}, \quad (3)$$

where $N(d)$ is the total number of droplets collected within the bin centered at d and N_s is the number of samples. The bin width is varied in d , starting from $6.25 \mu\text{m}$ and then increasing by a constant ratio 1.2. The reason for using wider bins for larger d is to reduce the fluctuations due to low numbers of larger droplets. Furthermore, it should be noted that the generation of droplets of size smaller than 2Δ for each mesh is quite likely not well captured in the present simulation. As a result, the droplets on the left of the dashed line ($d = 2\Delta$) are less trustworthy.

When the mesh size decreases, not only are more smaller droplets ($d \lesssim 50\mu\text{m}$) captured (which is as expected), but we also observe that more larger droplets ($d \gtrsim 100\mu\text{m}$) are collected. These large droplets ($d \gtrsim 100 \mu\text{m}$), such as those shown in Fig. 10, are typically generated from thicker ligaments, which are in turn produced by fingering at the end rim of the sheet (see Fig. 7) or holes-induced sheet rupture (see Fig. 8). If the mesh is not sufficiently fine to capture the Taylor-Culick rim at the edge of a liquid sheet (or at the edge of a hole) as shown in Fig. 6, then such a thick ligament may not get a chance to form. Instead, many tiny ligament will be produced due to numerical breakup. As a consequence, less large droplets appear in the M0 and M1 results.

The probability distribution function (PDF) of droplet number (P_n) and mass (P_m) are shown in Figs. 11(b) and (c), respectively, where P_n and P_m are defined as

$$P_n(d) = \frac{N(d)}{\Delta_d \sum N(d)} \quad (4)$$

and

$$P_m(d) = \frac{m(d)}{\Delta_d \sum m(d)} \quad (5)$$

where Δ_d is the bin width and $m(d)$ represent the total mass of droplets collected in the bin centered at d . Due to the fact that more smaller ($d \lesssim 50\mu\text{m}$) and larger droplets

($d \gtrsim 100\mu\text{m}$) are captured in fine mesh runs, P_n is more convex for the fine meshes than for the coarse meshes. In spite of the discrepancy for the smaller and larger droplets, the slopes of P_n (in a log-linear scale) for the four different meshes agree quite well for an intermediate range of droplet size between 50 to 100 μm . In general, P_n for M2 and M3 meshes agree reasonably well with each other, but are significantly different from the M0 and M1 results. The M3 PDFs are more noisy due to the shorter sampling time. To get a smoother PDF, the simulation has to be conducted for a longer time (for example, the M0 size distribution is much smoother than the others due to the longer sampling time). However, due to the extreme computational cost for the M3 mesh, this task can only be relegated to future works.

It is quite clear that the number of small droplets ($d \lesssim 50\mu\text{m}$) increases when the mesh is refined and thus is still mesh dependent, even for the finest mesh used here. However, these small droplets consist of only a small fraction of the total mass as shown in Fig. 11 (c). Compared to the droplet number distribution, for some applications the mass distribution is indeed more important in characterizing sprays. It is observed that the main contribution to the mass is from large droplets ($d \gtrsim 50\mu\text{m}$), which are well captured by the fine meshes like M2 and M3 used in the present study. The difference between the results of the fine and coarse meshes are more profound in P_m . The peaks for M0 and M1 are located at about 50-90 μm ; while those for M2 and M3 at about 180-230 μm . The shift toward the larger droplets is due to the fact that more larger droplets are captured by the finer meshes.

Finally, the Log-Normal and Gamma distribution functions are employed to fit the PDF. The Log-Normal distribution functions is given as

$$P_L(d) = \frac{1}{d\eta\sqrt{2\pi}} \exp\left[-\frac{(\ln d - \zeta)^2}{2\eta^2}\right], \quad (6)$$

where the mean and the variance of $\ln d$ are ζ and η^2 . The Gamma distribution can be expressed as

$$P_G(d) = \frac{\beta^\alpha}{\Gamma(\alpha)} d^{\alpha-1} \exp(-\beta d), \quad (7)$$

where $\alpha = (\hat{\zeta}/\hat{\eta})^2$ and $\beta = \alpha/\hat{\zeta}$, and the mean and variance of d are denoted as ζ' and η'^2 .

A comparison between the present simulation results and the PDF models are shown in Fig. 11(b) and (c). The Log-Normal distribution is fit with $\eta \simeq 1.2$ and $\zeta \simeq 2.5$; while the Gamma with $\alpha \simeq 1.2$ and $\beta \simeq 0.033$. The Log-Normal distribution is observed to match better the finer mesh results; while the Gamma distribution seems to fit better the coarser mesh results. The Log-Normal distribution has also been observed to well fit the droplet

size distribution in recent experiments⁷. Furthermore, it is interesting to notice that η measured experimentally varies from 1 to 1.8, which agrees well with that obtained in the present simulation.

In spite of the reasonable performance of the distribution models, the physical reasons behind are still not fully understood. The idea behind the Log-Normal model is that the formation of droplets is a sequential cascade of breakups, where the larger mother drops break into smaller daughter droplets. The ratio between the daughter and mother drops in each breakup is a random fractional number which follows a normal distribution. As a result, the size of the droplets formed at the end follows a Log-Normal distribution. In contrast to the breakup process, the coalescence between droplets introduces an inverse cascade, *i.e.*, smaller droplets collide and merge to form bigger droplets or the coalescence of the smaller blobs constitutive of a ligament forms bigger blobs. These aggregation scenarii will result in a Gamma distribution for the droplet size⁶. The simulations presented here show that the spray formation is through a sequence of different complex mechanisms, and neither of these two PDF models are therefore likely to completely capture these mechanisms. We have observed breakups in sequence, the bulk liquid first breaks into thin liquid sheets, then the sheets into fingers and ligaments, and at last the ligaments into droplets of different size. However, the process of spray formation is clearly not a sequence of random breakups like suggested in the Log-Normal model. (We rarely see a droplet, once formed, further break into smaller droplets in the fine mesh runs.) On the other hand, coalescences of droplets, the assumption behind the Gamma distribution model, are only occasionally observed. Therefore, it is also quite likely that the aggregation would not have a significant impact on the droplet size, either.

Notice that both of these classical distributions, the Log-Normal and the Gamma, are obtained when a scaling process is observed, that is when nonlinear effects occur over a large range of scales. For example, Kolmogorov turbulent cascade for the Log-Normal distribution, or Einstein-Smoluchowski aggregation dynamics for the Gamma distribution, both span over a wide range of scales from ℓ_{\min} to ℓ_{\max} . The fact that $\ln(\ell_{\max}/\ell_{\min})$ is large is a condition of applicability of the central limit theorem in these theories. Here the best fit to the Log-Normal indicates that $\ln(\ell_{\max}/\ell_{\min}) \sim 2\eta \approx 2.4$. Compared to many scaling observations performed in physics over a moderate range of scales, to be specific with just one decade as $\ln(\ell_{\max}/\ell_{\min}) \geq \ln 10 \approx 2.3$, the present system has a sufficiently large range of scales to

consider scaling hypotheses, but not yet a “truly” large range of scales as in Kolmogorov turbulent cascade experiments at the large Reynolds numbers. The absence of a truly large range of scales makes it difficult to draw definite conclusions from the fit of the droplet size probability distribution to the classical theories, but it also indicates that none of these theories is without doubt in its range of validity.

Another analysis of the droplet size distributions, that does not involve a single scaling process, is to consider several distinct processes at different scales, for instance “rim drops” from the disintegration of the Taylor-Culick rims and “film drops” from the disintegration of the thin sheets. In some experiments,⁴ hints of the bimodal distributions that would result from two distinct processes have been seen. We observe no such effects in our distributions, and believe that the oscillations of the M3 distribution are entirely explainable by the statistical effects of short sampling time, although further research may be necessary to confirm that.

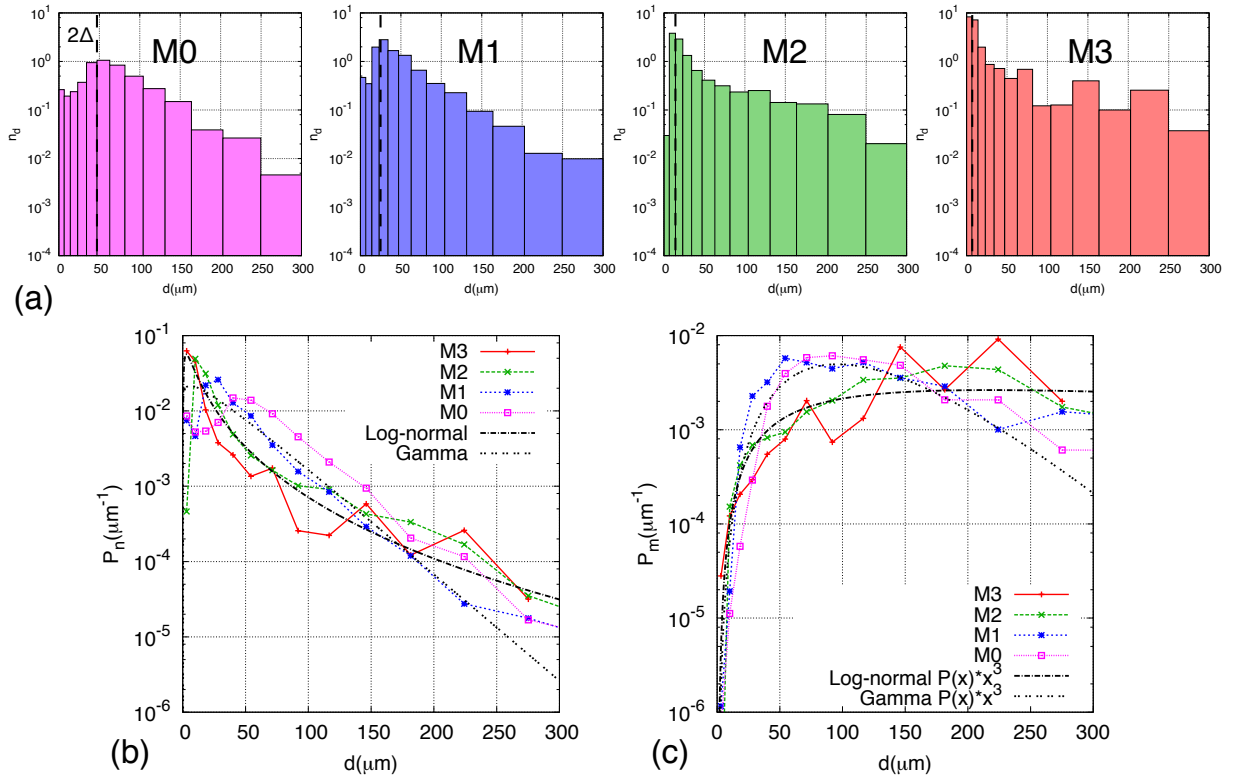


FIG. 11. The droplet size PDF obtained from different meshes (a) M3 (b) M2 and (c) M1 and (d) M0. The bin width for all the cases is $6.25 \mu\text{m}$. (e) Comparison of PDF profiles with Lognormal and Gamma distribution functions.

IV. CONCLUSIONS

Spray formation in a gas-liquid mixing layer is investigated by DNS in the present study. To examine whether the simulation fully resolves all the physical scales the mesh resolution is varied and the finest mesh consists of about 4 billion cells. The simulation results clearly show the detailed processes of how the bulk liquid jet breaks into sheets, then ligaments, and finally droplets. The development of the interfacial wave is crucial to the sheet formation. Both quasi-2D and fully 3D waves are observed. For the 3D waves, the development of the 3D structure is clearly much faster than the Rayleigh-Plateau instability in the end rim. Ligaments are shown to be generated by fingering at end rims of liquid sheets and also by expansion of holes in liquid sheets. The evolution of holes agrees well with the Taylor-Culick theory. Due to the interaction with the surrounding turbulent gas stream, ligaments generally exhibit irregular shapes and complex dynamics when they break into droplets. The size distributions of droplets in a sampling box at the downstream of the breaking wave is investigated for different meshes. It is found that a coarse mesh will not only miss the small droplets but also the larger ones. The reason is that if the development of the wave is not well resolved (the mesh is not sufficiently fine for the curvature of the wave crest or the shear layer above the wave), the sheet formation will be erroneous, resulting in fake breakups and many tiny ligaments and drops, instead of larger droplets and thicker ligament as observed in the fine mesh results. At the end, the Log-Normal and Gamma distributions are employed to fit the PDF data and the Log-Normal model seems to fit better with the simulation results of the fine meshes.

ACKNOWLEDGMENTS

This project has been supported by the ANR MODEMI project (ANR-11-MONU-0011) program, and the FIRST project supported by the European Commission under the 7th Framework Programme under Grant Agreement No. 265848. This work was granted access to the HPC resources of TGCC-CURIE and CINES-Occigen under the allocations 2015-x20152b7325 made by GENCI. We would also acknowledge PRACE (2014112610) for awarding us access to CINECA-FERMI and to LRZ-SuperMUC based in Italy and Germany.

REFERENCES

- ¹J. C. Lasheras and E. J. Hopfinger, “Liquid jet instability and atomization in a coaxial gas stream,” *Annu. Rev. Fluid Mech.* **32**, 275–308 (2000).
- ²J. Eggers and E. Villermaux, “Physics of liquid jets,” *Rep. Prog. Phys.* **71**, 036601 (2008).
- ³E. Villermaux, P. Marmottant, and J. Duplat, “Ligament-mediated spray formation,” *Phys. Rev. Lett.* **92**, 074501 (2004).
- ⁴P. Marmottant and E. Villermaux, “On spray formation,” *J. Fluid Mech.* **498**, 73–111 (2004).
- ⁵J. Hoepffner, R. Blumenthal, and S. Zaleski, “Self-similar wave produced by local perturbation of the kelvin-helmholtz shear-layer instability,” *Phys. Rev. Lett.* **106**, 104502 (2011).
- ⁶E. Villermaux, “Fragmentation,” *Annu. Rev. Fluid Mech.* **39**, 419–446 (2007).
- ⁷L. Opfer, I. V. Roisman, J. Venzmer, M. Klostermann, and C. Tropea, “Droplet-air collision dynamics: Evolution of the film thickness,” *Phys. Rev. E* **89**, 013023 (2014).
- ⁸J. O. Marston, T. T. Truscott, N. B. Speirs, M. M. Mansoor, and S. T. Thoroddsen, “Crown sealing and buckling instability during water entry of spheres,” *J. Fluid Mech.* **794**, 506–529 (2016).
- ⁹J.-P. Matas, S. Marty, and A. Cartellier, “Experimental and analytical study of the shear instability of a gas-liquid mixing layer,” *Phys. Fluids* **23**, 094112 (2011).
- ¹⁰J. J. S. Jerome, S. Marty, J.-P. Matas, S. Zaleski, and J. Hoepffner, “Vortices catapult droplets in atomization,” *Phys. Fluids* **25**, 112109 (2013).
- ¹¹J.-P. Matas, S. Marty, M. S. Dem, and A. Cartellier, “Influence of gas turbulence on the instability of an air-water mixing layer,” *Phys. Rev. Lett.* **115**, 074501 (2015).
- ¹²D. Fuster, J. P. Matas, S. Marty, S. Popinet, H. J., A. Cartellier, and S. Zaleski, “Instability regimes in the primary breakup instability regimes in the primary breakup instability regimes in the primary breakup region of planar coflowing sheets,” *J. Fluid Mech* **736**, 150–176 (2013).
- ¹³M. Gorokhovski and M. Herrmann, “Modeling primary atomization,” *Annu. Rev. Fluid Mech.* **40**, 343–366 (2008).
- ¹⁴R. Lebas, T. Menard, P. A. Beau, A. Berlemont, and F.-X. Demoulin, “Numerical simulation of primary break-up and atomization: Dns and modelling study,” *Int. J. Multiphase*

- Flow **35**, 247–260 (2009).
- ¹⁵J. Shinjo and A. Umemura, “Simulation of liquid jet primary breakup: Dynamics of ligament and droplet formation,” *Int. J. Multiphase Flow* **36**, 513–532 (2010).
- ¹⁶G. Tryggvason, R. Scardovelli, and S. Zaleski, *Direct numerical simulations of gas-liquid multiphase flows* (Cambridge University Press, 2011).
- ¹⁷M. Rudman, “A volume-tracking method for incompressible multifluid flows with large density variations,” *Int. J. Numer. Meth. Fluids* **28**, 357–378 (1998).
- ¹⁸S. Popinet, “An accurate adaptive solver for surface-tension-driven interfacial flows,” *J. Comput. Phys.* **228**, 5838–5866 (2009).
- ¹⁹M. M. Francois, S. J. Cummins, E. D. Dendy, D. B. Kothe, J. M. Sicilian, and M. W. Williams, “A balanced-force algorithm for continuous and sharp interfacial surface tension models within a volume tracking framework,” *J. Comput. Phys.* **213**, 141–173 (2006).
- ²⁰Y. Ling, S. Zaleski, and R. Scardovelli, “Multiscale simulation of atomization with small droplets represented by a lagrangian point-particle model,” *Int. J. Multiphase Flow* **76**, 122–143 (2015).
- ²¹T. J. Arrufat, S. Dabiri, D. Fuster, Y. Ling, L. Malan, R. Scardovelli, G. Tryggvason, P. Yecko, and S. Zaleski, “The PARIS-Simulator code.” Available from <http://www.lmm.jussieu.fr/~zaleski/paris/index.html>.
- ²²I. V. Roisman, K. Horvat, and C. Tropea, “Spray impact: rim transverse instability initiating fingering and splash, and description of a secondary spray,” *Phys. Fluids* **18**, 102104 (2006).
- ²³G. Agbaglah, C. Josserand, and S. Zaleski, “Longitudinal instability of a liquid rim,” *Phys. Fluids* **25**, 022103 (2013).
- ²⁴P. Yecko and S. Zaleski, “Transient growth in two-phase mixing layers,” *J. Fluid Mech.* **528**, 43–52 (2005).